Supplementary Information for

Direct observation of room-temperature exciton condensation

Jiaxin Yu[1,2,*], Guangyu Dai[1,2], Shuai Xing[1,2], Weiwei Zhang[1], Lin Dou[1], Tianci Shen[1], Xinyu Zhang[1], Xialian Feng[1] & Fuxing Gu[1,*]

[1]Laboratory of Integrated Opto-Mechanics and Electronics, School of Optical-Electrical and Computer Engineering, University of Shanghai for Science and Technology, Shanghai, China.

[2]These authors contributed equally: Jiaxin Yu, Guangyu Dai, Shuai Xing.

*Corresponding authors, e-mail: yujiaxin@usst.edu.cn (J. Y.); gufuxing@usst.edu.cn (F. G.).

CONTENTS

Supplementary Text

S1. Three-capacitor coupling model.

A sufficiently strong electric field E can polarize excitons, reduce their energy through the dc Stark effect, and drive them toward regions of stronger electric fields, thereby creating a confinement potential:

$$U(x) = -\frac{1}{2}\alpha E(x)^2, \text{(S1)}$$

where α is the exciton polarizability. To quantitatively evaluate E between material and substrate, we treat the tip–material–substrate stack as three capacitances in series (Extended Data Fig. 2a): one between the material and substrate with capacitance density $C_{\mathrm{ms}} = \varepsilon_0/z(x)$, and one between the tip and material $C_{\mathrm{tm}} = \varepsilon_0/d_{\mathrm{tip}}$ (with tip spacing $d_{\mathrm{tip}} = \mathrm{const.}$). Additionally, for atomically thin materials, the charge storage per unit area is not limited by the vacuum gap but also constrained by the finite density of states (DOS) of the layer. This effect is captured by the quantum capacitance $C_{\mathrm{q}} = e^2\cdot\mathrm{DOS}$[1], which relates an incremental sheet charge dQ to the shift of the Fermi level dμ inside the material ($\mathrm{d}\mu = \mathrm{d}Q/C_{\mathrm{q}}$) without generating an additional spatial electric field within the monolayer.

During measurements, the tip bias is adjusted until the first-harmonic electrostatic force is nulled:

$$V_{\mathrm{tip}} - V_{\mathrm{mat}} = \Delta\phi_{\mathrm{tm}} / e, \text{(S2)}$$

Here, $\Delta\phi_{\mathrm{tm}}/e = (\phi_{\mathrm{tip}} - \phi_{\mathrm{mat}})/e$ is applied to C_{tm} (Extended Data Fig. 2a). Meanwhile, the work-function difference between the material and the substrate, $\Delta\phi_{\mathrm{ms}} = \phi_{\mathrm{mat}} - \phi_{\mathrm{sub}}$, is divided between the C_{q} drop and the C_{ms} vacuum-gap drop, i.e.,

$$\Delta\phi_{\mathrm{ms}} / e = V_{\mathrm{q}} + V_{\mathrm{ms}} = \frac{Q}{C_{\mathrm{q}}} + \frac{Q}{C_{\mathrm{ms}}}, \text{(S3)}$$

where $V_{\mathrm{q}} = Q/C_{\mathrm{q}}$ denotes a chemical-potential voltage. In a two-dimensional semiconductor, the additional sheet charge Q does not produce a classical Coulomb potential drop within the atomic layer; instead, it shifts the electronic chemical potential with respect to the vacuum level. The monolayer is regarded as electrically floating. Charge conservation in the series pair ($C_{\mathrm{q}} \parallel C_{\mathrm{ms}}$) gives the material–substrate voltage by

$$\Delta V_{\mathrm{ms}}(z) = \frac{\Delta\phi_{\mathrm{ms}} / e}{1 + C_{\mathrm{ms}} / C_{\mathrm{q}}} = \frac{\Delta\phi_{\mathrm{ms}} / e}{1 + \varepsilon_0 / zC_{\mathrm{q}}}, \text{(S4)}$$

It can be related to the contact potential via

$$V_{\mathrm{CPD}}(z) = \Delta\phi_{\mathrm{tm}} / e + V_{\mathrm{sub}} + \Delta V_{\mathrm{ms}}(z), \text{(S5)}$$

Using the calibrated value of $\phi_{\mathrm{tip}} = 4.943 \pm 0.025$ eV (in agreement with the vendor specification 4.9 eV), the work-function of the nanostructured Au ϕ_{sub} is measured to be 4.698 ± 0.006 eV, slightly lower than that of bulk Au ($\phi_{\mathrm{Au}} \approx 5.1$ eV). The potential of the substrate can then be derived from the contact potential of the area of bare Au:

$$V_{\mathrm{sub}} = V_{\mathrm{CPD\_sub}} - \frac{\phi_{\mathrm{tip}} - \phi_{\mathrm{sub}}}{e}, \text{ (S6)}$$

Combining Eq. (S5) with Eq. (S6),

$$V_{\mathrm{CPD}}(z) - V_{\mathrm{CPD\_sub}} = \varDelta V_{\mathrm{ms}}(z) - \varDelta\phi_{\mathrm{ms}} / e, \text{ (S7)}$$

The left part of Eq. (S7) is defined as $\varDelta V_{\mathrm{CPD}}(z) \equiv V_{\mathrm{CPD}}(z) - V_{\mathrm{CPD\_sub}}$, which can be directly extracted from the SKPM map, while the right part involves $\varDelta\phi_{\mathrm{ms}}$ and C_{q}, which are the key parameters to be obtained from data.

The above model is applied to correlate the measured V_{CPD} with the interlayer separation z. Using the morphology and surface-potential maps (e.g., Fig. 1c,d in the main text), we extracted dozens of cross-sectional profiles $\varDelta V_{\mathrm{CPD}}(x, y)$ and $z(x, y)$ to construct the $\varDelta V_{\mathrm{CPD}}(z)$ scatter plot (Fig. 1F in the main text). The global fit yields a quantum capacitance $C_{\mathrm{q}} = 0.03 \pm 0.01$ mF m^{-2}, indicating that the material remains essentially intrinsic[2]. The value of $\varDelta\phi_{\mathrm{ms}}$ is 178 ± 18 meV, corresponding to ϕ_{mat} of 4.81 eV, in good agreement with the intrinsic work function of $\mathrm{WSe_2}$ ($\phi_{\mathrm{WSe2}} \sim 4.7$ eV). The global fit reproduces the data well for large separations z (e.g., $z > 50$ nm), whereas it deviates markedly at small z (Extended Data Fig. 2b). We attribute this deviation to the field-induced doping: when the material–substrate separation becomes extremely small, the strongly enhanced electric field drives carriers into the monolayer, shifts the Fermi level into the band, enlarges the density of states, and thereby raises the quantum capacitance C_{q}. The resulting increase in C_{q} manifests itself as a pronounced sensitivity of the contact potential to interlayer spacing. At the centre of the potential trap, where the gap is minimal, the contact potential varies much more steeply than the topography, and a similar sharp variation is also observed in the region outside the trap. $C_{\mathrm{q}} = 3$ mF m^{-2} provides the best fit for the rapidly varying region with $z < 10$ nm, implying a substantial enhancement of the electric field at the trap centre. We therefore adopt the fitting parameters obtained in the central region for the quantitative description of the trap, because cold excitons are confined mainly to the vicinity of the trap centre.

The electric field E between the material and the substrate can then be calculated by:

$$E(x) = \frac{\varDelta V_{\mathrm{ms}}(x)}{z(x)}, \text{ (S8)}$$

By fitting the experimental data with Eqs. (S4) and (S7), we obtained $\varDelta\phi_{\mathrm{ms}}$ in the range of 200–400 meV depending on the material, and C_q values of 0.03–0.1 mF m^{-2} at $z > 20$ nm and ~3 mF m^{-2} at $z < 10$ nm (Extended Data Fig. 2b). The latter value is used for calculating ΔV_{ms} and E in Fig. 1g.

The spatial variation of E is clearly reflected in the Raman-intensity maps (Extended Data Fig. 4i): the intensity of the $E' + A'$ and 2LA modes is strongest at the rim of the trap and gradually weakens toward its centre. Because a Raman image records the light–matter scattering matrix element, $I_{Raman} \propto n_{ph}(T)\ |p(E)|^2$, where the phonon occupation $n_{ph}(T)$ is essentially uniform at room temperature, the intensity distribution should originate from a spatial modulation of the dipole moment $p(E)$. Since p is proportional to the overlap between the electron and hole wavefunctions i.e., $p(E) \propto \langle \psi_e | \psi_h \rangle$, a strong E separates the electron and hole wavefunctions through the quantum-confined Stark effect, thereby reducing their overlap. Consequently, the suppressed Raman scattering at the trap centre confirms a strong local E, whereas the enhanced intensity at the rim indicates a weaker field.

S2. MAM system for observing excitonic dynamics.

S2.1 Collection efficiency and magnification

In a conventional far-field system, the detection angle is limited by the objective NA. Even with a 100×/NA = 0.9 objective, the half-angle is 64°. This narrow cone severely limits the collection of exciton emission: simulations (Fig. S1a,b) yield detectable fractions of only 25.9% for out-of-plane dipoles and 53.6% for in-plane dipoles. By contrast, a SiO_2 microsphere (refractive index ≈ 1.46) converts high-k in-plane components into the far field and dramatically enhances the collection efficiency. In MAM, up to 80.0% (out-of-plane) and 94.1% (in-plane) can be collected with a 50×/NA = 0.55 objective (Fig. S1c,d), enabling direct imaging of exciton dynamics.

The magnification (M) is calibrated using the pit spacing of a gold-coated optical disc. AFM gives 1.56 ± 0.06 µm (Extended Data Fig. 7a), while MAM gives 4.06 ± 0.88 µm (Extended Data Fig. 7b), corresponding to $M = 2.60 \pm 0.56$, consistent with ref[3,4]. With this M, the object-space FOV for a 6.5-µm microsphere is 2.5–2.8 µm in diameter in the object plane, comparable to the geometric footprint of the microsphere in the virtual image.

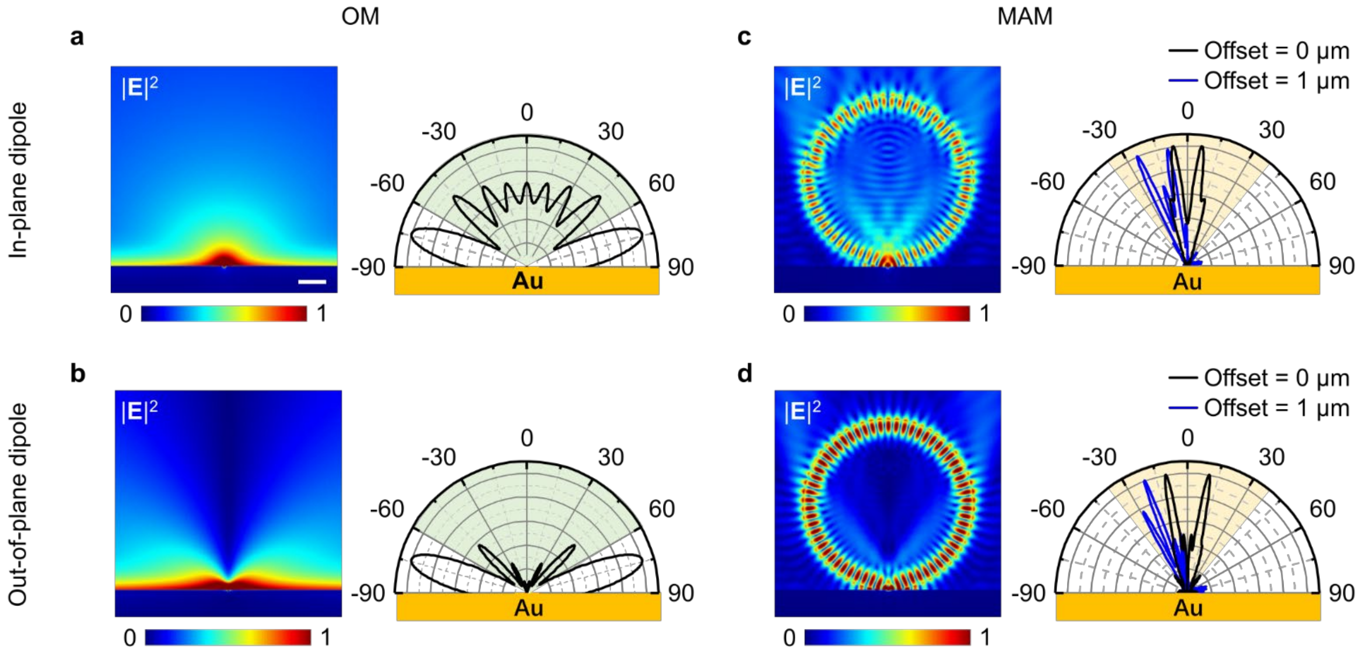

Fig. S1. Collection of dipoles in OM and MAM. a,**b**, Conventional OM with a NA = 0.9 objective: simulated field-intensity maps $|\mathbf{E}|^2$ above Au (left) and collected power versus angle (right; shaded green, NA cone) for in-plane (**a**) and out-of-plane dipoles (**b**). Collection efficiency: 53.6% (in-plane), 25.9% (out-of-plane). **c**,**d**, MAM with a NA = 0.55 objective: field maps (left) and collected power versus angle (right; shaded orange, NA cone) for in-plane (**c**) and out-of-plane dipoles (**d**). Black curves, dipole at trap centre; blue curves, at trap rim (offset 1 μm). Efficiency rises to 94.1% (in-plane) and 80.0% (out-of-plane). Scale bar, 1 μm (**a**).

S2.2 Coherence measurement

Far-field PL images acquired with MAM directly reveal coherence: clear concentric interference rings appear around the microsphere when coherence is high. Rings consistently appear for WSe_2/Au systems (Extended Data Fig. 6g), but are absent for WSe_2/SiO_2 systems where SPPs are not supported (Extended Data Fig. 6h). The effect is independent of cavity quality: even WSe_2/Au systems with broad WGMs still produce rings on WSe_2/Au (e.g., 2–4 μm spheres). As a counterexample, $MoSe_2$/Au systems exhibit no rings (Extended Data Fig. 6i). Comparing the exciton structures and radiative channels of these three systems indicates that the emergence of spatial coherence requires both a densely populated dark-exciton reservoir and an efficient radiative channel.

To pinpoint the spectral origin, we spectrally filter the WSe_2/Au emission into two bands—one near the bright-exciton line (~1.665 eV, bright band) and one near the dark-exciton line (~1.625 eV, dark band)—and record their far-field PL images separately (Fig. S2). The dark band exhibits concentric rings irrespective of resonance with microsphere WGMs, indicating that its coherence arises from spontaneous emission of dark excitons. By contrast, the bright band shows rings only when resonant with a WGM and shows no ring-like coherence when detuned. The strong dependence of bright-band coherence on Purcell enhancement therefore suggests that it does not originate from spontaneous emission of bright excitons alone, but is more likely to arise from phonon-assisted up-conversion of a condensed dark-exciton reservoir that feeds the bright channel[5,6].

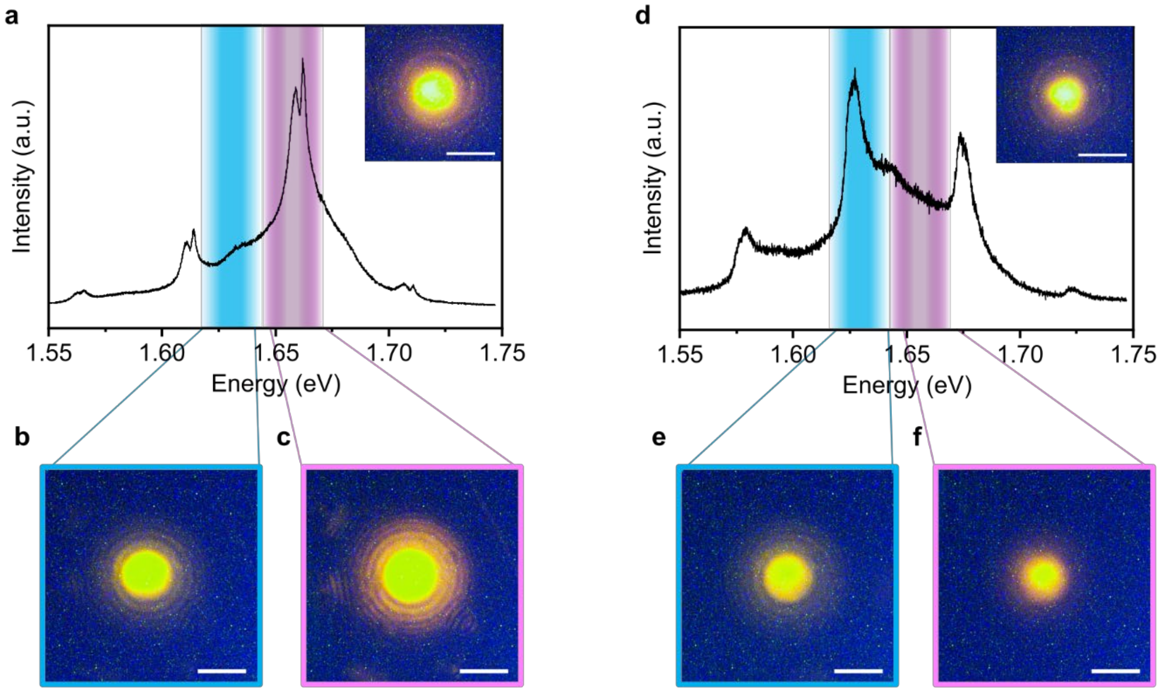

Fig. S2. Spectrally resolved far-field coherence from WSe_2/Au. **a–c,** With the WGM peak near the bright-exciton line (**a**), both band-passes [bright: 1.642–1.664 eV (magenta), dark: 1.620–1.642 eV (cyan)] show concentric interference rings (**b**,**c**), evidencing coherence. **d–f,** With the WGM peak near the dark-exciton line (**d**), coherence appears only in the dark-band channel (**e**), while the bright-band channel shows no rings (**f**). Scale bars, 5 μm.

Notably, two factors are critical for the measurement. The first is defocus, which broadens the PSF. As shown in Fig. S3, interferograms taken at best focus and with a controlled defocus $\delta z \approx 252 \pm 17$ nm exhibit markedly different fringe extents. To avoid conflating defocus with extended coherence, identical focus conditions are maintained for all comparisons (pump-dependence in Fig. 3 and on-/off-axis in Fig. 4). Best-fit defocus values in Extended Data Fig. 8 are small: $\delta z \approx 251 \pm 84$ nm for OM and $\delta z \approx 126 \pm 8$ nm for MAM—both well within the system depth of field (i.e., 750 nm for MAM). The second is WGMs. If the detection band includes a WGM, weak leakage near the equatorial plane produces an annular bright ring immediately outside the FOV. However, these WGM-induced fringes occur only when a high-Q WGM lies within the collection window and appear outside the FOV of MAM (Extended Data Fig. 9a–c). By contrast, fringes of excitonic origin are confined within the FOV and persist even when WGMs are excluded from the detection band (Extended Data Fig. 9d–f). The additional momentum carried by WGMs also distorts the fringe phase along the annulus, as evident in phase retrieval.

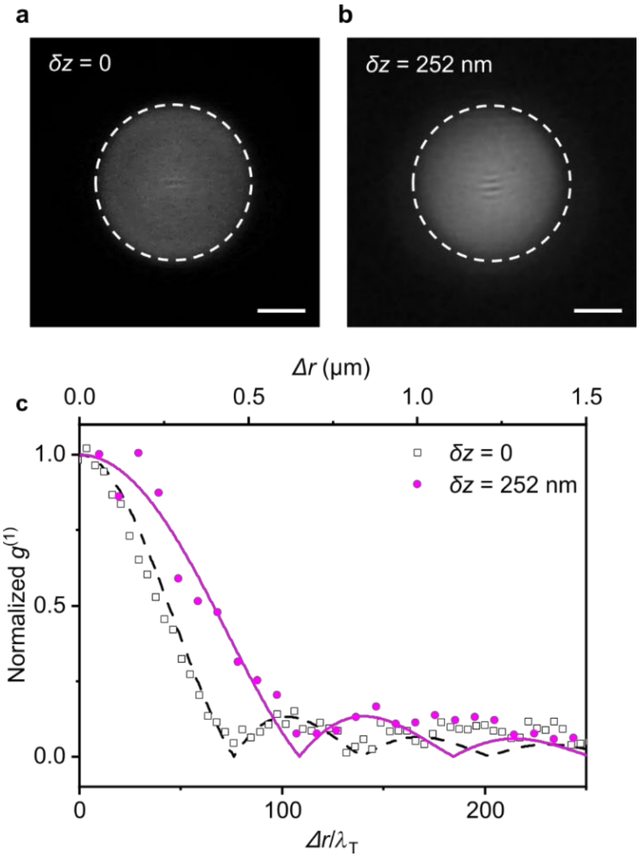

Fig. S3. Effect of defocus on spatial-coherence retrieval with MAM. a,b, Point-inversion interferograms at best focus ($\delta z = 0$, **a**) and with $\delta z = 252$ nm defocus (**b**). Dashed circles mark the FOV. Scale bars, 2 μm (**a,b**). **c,** Radial profiles under two conditions with fits to the *f* function.

S3. Lifetime of dark excitons.

The dark-exciton lifetime is a key parameter for analysing exciton populations. Simulations of total and radiative decay for in-plane and out-of-plane dipoles (Fig. S4a) show that on a SiO_2/Si substrate, both orientations decay at their intrinsic rates, with no evidence of substrate-induced acceleration. On Au, the total decay (quantified by Purcell factors F_{P_total}) of both orientations is enhanced, whereas the radiative channel (quantified by F_{P_rad}) of in-plane dipoles is strongly suppressed.

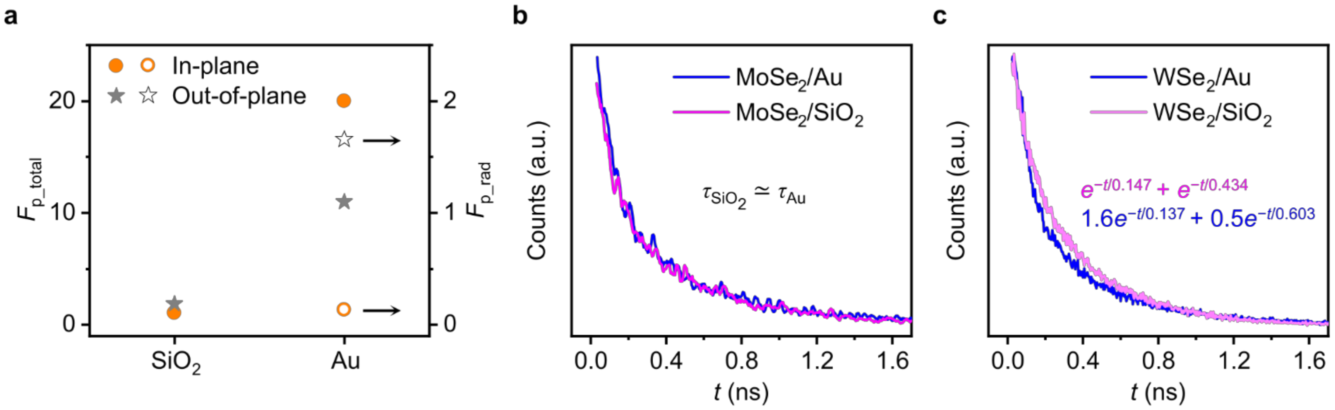

Fig. S4. Dark-exciton lifetimes. a, Simulated Purcell factors (F_P) for in-plane and out-of-plane dipoles near SiO_2 and Au substrates. On SiO_2, the total (F_{P_total}) and radiative Purcell factors (F_{P_rad}, data not shown) are close to unity for both orientations. On Au, F_{P_total} is enhanced for both types of dipoles (solid symbols), whereas F_{P_rad} for the in-plane dipole is significantly suppressed (open circle). **b,** TRPL of monolayer $MoSe_2$ on SiO_2 ($MoSe_2/SiO_2$) and on Au ($MoSe_2$/Au), showing identical lifetimes. **c,** TRPL of monolayer WSe_2 on SiO_2 (WSe_2/SiO_2) and on Au (WSe_2/Au) with bi-exponential fits, revealing a conversion of the long-time component into a short-time one on Au.

We therefore compared room-temperature time-resolved photoluminescence (TRPL) of monolayer $MoSe_2$ and WSe_2 on the two substrates using a lateral heterostructure in which a single flake bridges the SiO_2/Si and Au regions (main-text Fig. 1c), thereby eliminating sample variability. For $MoSe_2$, the TRPL traces on the two substrates nearly overlap (Fig. S4b), indicating the absence of any substrate-induced lifetime modification and no additional slow component attributable to dark excitons. This is consistent with the simulations, which show that the bright in-plane channel is quenched on Au, and with the low population of dark excitons in $MoSe_2$. For WSe_2, the region on Au exhibits a shorter lifetime than that on SiO_2/Si (Fig. S4c). Bi-exponential fitting ($t_1 \approx 150$ ps, $t_2 \approx 500$ ps) shows that the fraction of the short component (t_1) increases from approximately 50% to 70% on Au.

Because WSe_2 hosts a substantial dark-exciton reservoir with an out-of-plane dipole, the combination of (i) the simulated metal-assisted enhancement and (ii) the acceleration of the long component on Au indicates that t_2 corresponds to dark-exciton emission. The increased t_1 thus results from the faster decay of this long component. In $MoSe_2$, where dark excitons are weakly populated, this effect is negligible. We thus determine the intrinsic dark-exciton lifetime $\tau_D \approx 500$ ps, which can be locally shortened in the near field of Au.

S4. The rate equation model.

To quantify how the excitation geometry controls the exciton distribution, we solve the steady-state rate equations (Fig. S5), with parameters detailed in Supplementary Table 1. Bright excitons are directly injected, whereas dark excitons are formed exclusively through Γ-point chiral optical-phonon-assisted spin flips of bright excitons[7,8]. At 300 K, the equilibrium phonon population gives a dark-to-bright conversion time that is 2–3 times slower than the reverse process. Accordingly, the coupled steady-state equations read

$$\partial_t n = I + D\nabla^2 n_B - \mu\nabla(n_B \nabla \mathbf{U}) - \frac{n_B}{\tau_B} - \frac{n_B}{\tau_{BD}} + \frac{n_D}{\tau_{DB}} - n_B^2 \gamma_B = 0\,, \text{(S9)}$$

$$\partial_t n_D = D\nabla^2 n_D - \mu\nabla(n_D \nabla \mathbf{U}) - \frac{n_D}{\tau_D} + \frac{n_B}{\tau_{BD}} - \frac{n_D}{\tau_{DB}} - n_D^2 \gamma_D = 0\,, \text{(S10)}$$

The coordinate origin is set at the centre of the trap potential, and pump photons follow a Gaussian spatial profile $I(x,y) = I_0 \exp(-\frac{(x-x_0)^2}{2\sigma^2} - \frac{(y-y_0)^2}{2\sigma^2})$ with a waist width σ centred at (x_0, y_0). As the exciton generation rate is given by $R = \iint I(x,y)dxdy = \frac{Pad}{h\nu}$, $I_0 = \frac{Pad}{h\nu(2\pi\sigma^2)}$. For simplicity, we analyse a 1D profile at $y = 0$, thus defining $I(x)= I(x, 0)$ and U(x) as obtained in Section 1. Solving Eq. (S9)–(S10) yields the spatial distributions of both bright and dark excitons. As shown in Extended Data Fig. 10a,b, with the trap in place, the total particle density rises significantly relative to the spatially uniform case in both excitation regimes, demonstrating the trap's strong capability to collect excitons.

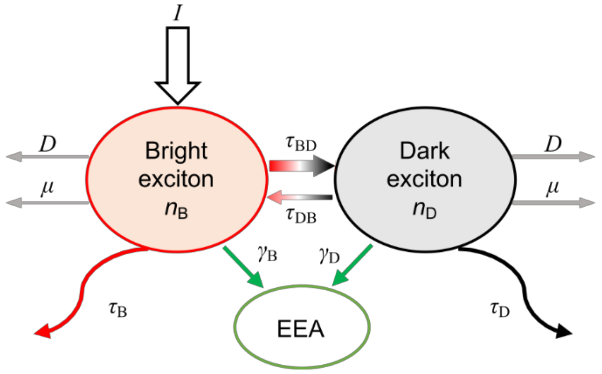

Fig. S5. Drift–diffusion rate-equation model. Parameters: n_B, bright-exciton density; n_D, dark-exciton density; I, optical injection; D, diffusion coefficient; μ, mobility; τ_{BD} (τ_{DB}), bright to dark (dark to bright) conversion time; τ_B (τ_D), lifetime of bright (dark) excitons; γ_B (γ_D), EEA rate of bright (dark) excitons.

The contrasting exciton redistribution under on-axis and off-axis excitation is readily captured by our rate-equation model. At room temperature, ultrafast (sub-picosecond) phonon-assisted interconversion between bright and dark excitons maintains thermal equilibrium between the two species on timescales far shorter than their decay lifetimes. Although CW pumping steadily injects non-equilibrium excitons, their transient excess population remains negligible relative to the thermalised population. The rapid X_B↔X_D conversion competes with several loss channels—most notably Auger-like exciton–exciton annihilation (EEA) and long-range transport—producing markedly different spatial distributions.

Under on-axis excitation, the laser spot is centred at the minimum of the trap potential. The resulting high exciton injection rate elevates the X_B density until the EEA rate (10^{-2}–10^{-1} cm^2 s^{-1})[9-11] becomes comparable to the spin-flip conversion rates. Consequently, a substantial fraction of X_B annihilates before converting into

X_D, limiting the supply of cold X_D that can thermalise and accumulate (Extended Data Fig. 10c). Enhanced Auger scattering not only depletes heat-carrying X_B but also generates hot phonons, which are promptly reabsorbed by the remaining excitons in the trap. Both thermalisation and accumulation of X_D near the trap are therefore strongly suppressed.

Under off-axis excitation, the trap can no longer confine excitons within the excitation spot. Short-lived X_B recombines rapidly near the excitation spot, whereas long-lived X_D can drift and diffuse into the trap, enabling efficient capture with minimal loss (Extended Data Fig. 10d). This scenario—short-lived X_B confined to the excitation spot and long-lived X_D accumulating at the trap centre—explains the distinct condensation behaviours observed experimentally.

The exciton degeneracy density is given by $n_k = m_X k_B T/(2\pi\hbar^2)$. For monolayer WSe_2 at 300 K, the above rate-equation model predicts a peak density $n_k \approx 10^{12}$ cm^{-2} at the threshold of P_{th0}. Approximating the bottom of the trap as a 2D isotropic harmonic oscillator with angular frequency $\omega = \sqrt{}(U''(0)/m_X)$, the critical particle number for a Berezinskii-Kosterlitz-Thouless (BKT) transition is given by $N_c = \pi(k_B T)^2/(6h^2\omega^2)^{12}$. This corresponds to an average density $n_{BKT} \approx 8\times10^{12}$ cm^{-2} and requires a pump power of >100 P_{th0}—two orders of magnitude higher than the degeneracy threshold—consistent with our experimental observations. The value of n_{BKT} is also quantitatively in agreement with the n value derived from the measured η as $\eta = \frac{1}{n\lambda_T^2}$. Notably, the calculated thresholds $P_{th0} \approx$ 1–10 μW exceed the measured values, probably because the model assumes an average diffusion coefficient of 10 cm^2 s^{-1}, whereas in reality it may vary by up to two orders of magnitude depending on the local density[13,14].

S5. Phonon-dominant thermalisation regime.

The spatial cooling behaviour depends on how excitons scatter with other quasiparticles in 2D materials, primarily with phonons and other excitons. At room temperature, the high phonon population strongly enhances the exciton–phonon coupling. In TMDs, the Huang-Rhys factor is S ≈ 1[15], indicative of Franck–Condon-type ultrastrong coupling. Consequently, a single exciton can shed its excess kinetic energy by emitting optical or interface phonons, rapidly approaching the 1*s* bound state. A single exciton–phonon scattering event occurs within τ_{EP} = 10–100 fs, while a full cascade to the 1*s* level takes τ_{th} = 50–200 fs[16], setting the baseline timescale for phonon-mediated thermalisation. Exciton–exciton scattering channels are far slower: even at 10^{12} cm^{-2}, the elastic coefficient is $\gamma_{EE} \approx 2 \times 10^{-12}$ meV cm^2, giving $\tau_{EE} \approx 3$ ps; the room-temperature annihilation coefficient is only $\gamma_{EEA} \approx 0.03$ cm^2 s^{-1} [10], corresponding to 33 ps at the same density. We therefore adopt a phonon-driven thermalisation model under our conditions. For a 1.96-eV pump, the initial excess energy is 300 meV above the 1*s* exciton. The corresponding thermalisation length is $L_{\mathrm{th}} = \sqrt{D\tau_{\mathrm{th}}}$ = 10–100 nm, much shorter than the diffusion length $L_{\mathrm{diff}} = \sqrt{D\tau_{\mathrm{D}}} \approx 1$ µm.

We assume excitons are created at (x_0, 0) with energy $E(x_0) = E_{1s} + E_{\mathrm{k},0}$, where E_{1s} represents the 1*s* excitonic energy, and $E_{\mathrm{k},0}$ is the initial kinetic energy. Inside the trap, the potential energy $U(x_0)$ is converted into kinetic energy during downhill drift. Solving the energy-balance equation $\frac{dE_{\mathrm{k}}}{dx} = -\frac{E_{\mathrm{k}} - k_{\mathrm{B}}T_{\mathrm{L}}}{L_{\mathrm{th}}} + \frac{dU}{dx}$ yields

$$E_{\mathrm{k}}(x) = [(E_{\mathrm{k},0} - k_{\mathrm{B}}T_{\mathrm{L}}) + U(x_0) - U(x)]\exp(-\frac{|x - x_0|}{L_{\mathrm{th}}}) + k_{\mathrm{B}}T_{\mathrm{L}}, \quad \text{(S11)}$$

where the lattice temperature T_{L} = 300 K gives $k_{\mathrm{B}}T_{\mathrm{L}}$ = 26 meV. Equation S9 describes the cooling behaviour in two pump regimes.

When the laser is focused on the trap axis, it continuously injects a dense flux of hot bright excitons directly at the potential minimum. Their excess energy is released via emission of phonons, but in such a confined, highly populated region, the emitted phonons are rapidly reabsorbed (the hot-phonon bottleneck), and Pauli blocking further impedes energy dissipation. For simplicity, we neglect pump-induced phonon accumulation and lateral phonon diffusion, as both would further slow cooling inside the laser spot, intensify the bottleneck, and reinforce our conclusion. The delayed cooling suppresses the formation of a cold exciton reservoir, raises the condensation threshold to higher pump powers, and leaves a residual high-energy tail whose spontaneous-emission noise impairs long-range phase coherence—thereby lowering the likelihood of condensation under on-axis pumping.

Under off-axis excitation, excitons are generated approximately 0.7–1 µm away from the trap centre and migrate inwards. Along the path, their density is low; EEA is therefore negligible, while successive acoustic- and optical-phonon scattering events cool them to the lattice temperature. Because the excitation spot (radius ≈ 300 nm) and the phonon-scattering length (≈100 nm) are both much smaller than the pump–trap separation, pump-induced phonon accumulation and diffusion are negligible here. Cooling at the trap centre is still governed by single-scattering events in a low-phonon-density environment. The trap is thus predominantly fed by cold, long-lived dark excitons, enabling rapid accumulation and yielding a markedly lower condensation threshold.

Supplementary Table 1. Values of parameters used in modelling

Parameter	Definition	Value/unit
n_B (n_D)	Density of X_B (X_D)	
σ	Waist width of the pump	0.5/2 √ ln(2) μm
a	Absorption coefficient	4×10^5 cm^{-1} [ref.17]
τ_B (τ_D)	Lifetime of X_B (X_D)	100 ps (500 ps)
d	Thickness of a monolayer	1 nm
$h\nu$	Photon energy of pump lasers	1.96 eV
P	Pump power	
τ_{BD} (τ_{DB})	X_B to X_D (X_D to X_B) conversion time	0.1 ps (0.4 ps)[refs.7,8,18]
m_X	Exciton mass	0.50 m_e
α	Exciton polarizability	10 eV nm^2 V^{-2} [ref.19]
D	Diffusion rate	10 cm^2 s^{-1}
μ	Exciton mobility	500 cm^2 V^{-1} s^{-1} [refs.2,13]
γ_B (γ_D)	EEA coefficients of X_B (X_D)	10^{-2} cm^2 s^{-1} (10^{-4} cm^2 s^{-1}) [refs.9–11]

References

1. Luryi, S. Quantum capacitance devices. *Appl. Phys. Lett.* **52**, 501–503 (1988).
2. Zhang, H., Berthod, C., Berger, H., Giamarchi, T. & Morpurgo, A. F. Band filling and cross quantum capacitance in ion-gated semiconducting transition metal dichalcogenide monolayers. *Nano Lett.* **19**, 8836–8845 (2019).
3. Darafsheh, A., Walsh, G. F., Dal Negro, L. & Astratov, V. N. Optical super-resolution by high-index liquid-immersed microspheres. *Appl. Phys. Lett.* **101**, 141128 (2012).
4. Darafsheh, A., Limberopoulos, N. I., Derov, J. S., Walker, D. E. & Astratov, V. N. Advantages of microsphere-assisted super-resolution imaging technique over solid immersion lens and confocal microscopies. *Appl. Phys. Lett.* **104**, 061117 (2014).
5. Mueller, N. S. et al. Photoluminescence upconversion in monolayer WSe_2 activated by plasmonic cavities through resonant excitation of dark excitons. *Nat. Commun.* **14**, 5726 (2023).
6. Li, Z. et al. Emerging photoluminescence from the dark-exciton phonon replica in monolayer WSe_2. *Nat. Commun.* **10**, 2469 (2019).
7. Chen, H.-Y., Sangalli, D. & Bernardi, M. First-principles ultrafast exciton dynamics and time-domain spectroscopies: dark-exciton mediated valley depolarization in monolayer WSe_2. *Phys. Rev. Res.* **4**, 043203 (2022).
8. Wang, Z. et al. Intravalley spin-flip relaxation dynamics in aingle-layer WS_2. *Nano Lett.* **18**, 6882–6891 (2018).
9. Erkensten, D. et al. Dark exciton-exciton annihilation in monolayer WSe_2. *Phys. Rev. B* **104**, L241406 (2021).
10. Sortino, L., Gulmus, M., Tilmann, B., de, S. M. L. & Maier, S. A. Radiative suppression of exciton-exciton annihilation in a two-dimensional semiconductor. *Light:Sci. Appl.* **12**, 202 (2023).
11. Lee, Y. et al. Boosting quantum yields in two-dimensional semiconductors via proximal metal plates. *Nat. Commun.* **12**, 7095 (2021).
12. Kruger, P., Hadzibabic, Z. & Dalibard, J. Critical point of an interacting two-dimensional atomic Bose gas. *Phys. Rev. Lett.* **99**, 040402 (2007).
13. Kulig, M. et al. Exciton diffusion and halo effects in monolayer semiconductors. *Phys. Rev. Lett.* **120**, 207401 (2018).
14. Uddin, S. Z. et al. Neutral exciton diffusion in monolayer MoS_2. *ACS Nano* **14**, 13433–13440 (2020).
15. Li, D. et al. Exciton-phonon coupling strength in single-layer $MoSe_2$ at room temperature. *Nat. Commun.* **12**, 954 (2021).
16. Trovatello, C. et al. The ultrafast onset of exciton formation in 2D semiconductors. *Nat. Commun.* **11**, 5277 (2020).
17. Ermolaev, G. A. et al. Spectroscopic ellipsometry of large area monolayer WS_2 and WSe_2 films. *AIP Conf. Proc.* **2359**, 020005 (2021).
18. Danovich, M., Zólyomi, V., Fal’ko, V. I. & Aleiner, I. L. Auger recombination of dark excitons in WS_2 and WSe_2 monolayers. *2D Mater.* **3**, 035011 (2016).
19. Massicotte, M. et al. Dissociation of two-dimensional excitons in monolayer WSe_2. *Nat. Commun.* **9**, 1633 (2018).